JACS
JOURNAL OF THE AMERICAN CHEMICAL SOCIETY

ARTICLE

pubs.acs.org/jacs

Cu_2Se Nanoparticles with Tunable Electronic Properties Due to a Controlled Solid-State Phase Transition Driven by Copper Oxidation and Cationic Conduction

Shannon C. Riha, Derek C. Johnson, and Amy L. Prieto*

Department of Chemistry, Colorado State University, Fort Collins, Colorado 80523, United States

Supporting Information

ABSTRACT: Stoichiometric copper(I) selenide nanoparticles have been synthesized using the hot injection method. The effects of air exposure on the surface composition, crystal structure, and electronic properties were monitored using X-ray photoelectron spectroscopy, X-ray diffraction, and conductivity measurements. The current−voltage response changes from semiconducting to ohmic, and within a week a 3000-fold increase in conductivity is observed under ambient conditions. The enhanced electronic properties can be explained by the oxidation of Cu^+ and Se^{2-} on the nanoparticle surface, ultimately leading to a solid-state conversion of the core from monoclinic Cu_2Se to cubic $Cu_{1.8}Se$. This behavior is a result of the facile solid-state ionic conductivity of cationic Cu within the crystal and the high susceptibility of the nanoparticle surface to oxidation. This regulated transformation is appealing as one could envision using layers of Cu_2Se nanoparticles as both semiconducting and conducting domains in optoelectronic devices simply by tuning the electronic properties for each layer through controlled oxidation.

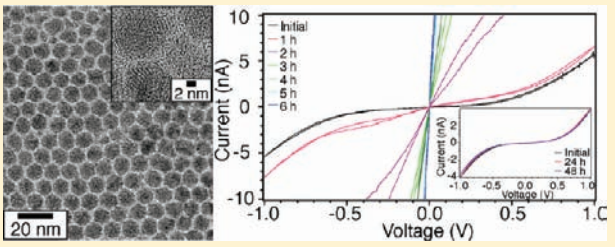

INTRODUCTION

Transition-metal chalcogenides are of current interest to energy-related research due to their semiconducting properties and the ability to tailor these properties through careful manipulation of the synthesis conditions. These materials have historically been made by energy-intensive and ultra-high-vacuum solid-state techniques that result in a high fabrication cost. Current research is therefore focused on developing wet-chemical methods for the synthesis of high-quality semiconducting nanomaterials as building blocks in optoelectronic devices.[1−4] Several solution-processed metal chalcogenide nanomaterials have been investigated as light-harvesting materials for photovoltaics, such as PbX (where X = S, Se, and Te),[5−8] Cu_2S,[9] $CuInS_2$,[10,11] $CuInSe_2$,[12,13] $CuIn_xGa_{1-x}Se$,[14,15] Cu_2ZnSnS_4,[16−19] and $Cu_2ZnSnSe_4$.[20] While the solution-based synthesis of these nanomaterials has been shown to be facile and applicable to a large class of compounds, the incorporation of such nanomaterials into fully functioning devices is not trivial.

A significant hurdle is that the surface of the chalcogenide nanomaterials is highly reactive due to the large number of unpassivated surface sites.[21] When exposed to oxygen, these surface sites often oxidize, thereby hindering their performance as a semiconducting material. This oxidation process is well documented, and a well-studied example is thin films of lead chalcogenide nanoparticles incorporated into photovoltaic devices.[5−8] In addition to the highly reactive surface, the large density of nanoparticle interfaces in thin films serve as energy barriers, drastically reducing the interparticle electrical conductivity in nanostructured devices.[22] Because of these hurdles, new and innovative methods are required for the synthesis, deposition, and stabilization of semiconducting metal chalcogenide nanoparticles for device integration.

One way to overcome some of these limitations is to control the resistance of a nanostructured film. Tricoli and Pratsinis accomplished this by depositing films containing both semiconducting and conducting nanomaterials such as n-type SnO_2 and p-type CuO, respectively.[22] The conductive material therefore serves as nanoelectrodes that reduce the high film resistance, thereby lowering the electrical conductivity losses found in most nanoparticle films. However, this method requires the use of materials with different electronic structures, and thus, proper band alignment must be taken into consideration when the semiconducting and conducting domains are chosen. To circumvent this, we have developed an approach to implement the same material as both the semiconducting and conducting domains by controllably tuning the electronic properties of Cu_2Se nanocrystals through time-resolved oxidation.

Stoichiometric Cu_2Se and nonstoichiometric $Cu_{2-x}Se$ are p-type semiconductors that can exist in many different crystallographic systems including orthorhombic, monoclinic, and cubic.[23,24] The optoelectronic properties of this material are

Received: July 14, 2010
Published: October 29, 2010

dx.doi.org/10.1021/ja106254h | J. Am. Chem. Soc. 2011, 133, 1383–1390

promising, and potentially tunable, due to the wide range of possible crystal structures, particle sizes, and corresponding band gaps.[24−29] The band gap energy for both Cu_2Se and $Cu_{2-x}Se$ is in the optimal range for use as an absorber material in photovoltaic devices. However, a widely varying indirect band gap of 1.1−1.5 eV[27,30,31] has been reported with a direct band gap between 2.0 and 2.3 eV.[27,31,32] While it has been shown that conductivity increases with increasing temperature, typical semiconducting behavior, many researchers also report observing an ohmic-type response.[27,33−45] The wide range in observed band gap energies and varying electronic behaviors are likely due to differences in the Cu to Se stoichiometry, recombination sites due to dislocations, large grain size distributions in polycrystalline films, size effects, and/or the oxidation state of the Cu and Se.[46] Cu_2Se contains Cu in the +1 oxidation state, while the substoichiometric analogue consists of multivalent Cu. When stoichiometric Cu_2Se is exposed to air under ambient conditions, Cu^+ oxidizes to Cu^{2+}, forming a surface oxide. In bulk crystals, and most thin films, the effects of surface oxidation are negligible. However, the effect is much more profound for nanoparticles because the surface-to-volume ratio is large. The surface oxidation can therefore significantly alter the physical and/or electronic properties of the material. We aim to take advantage of this process and use it to controllably tune the electronic properties of the material. As demonstrated in the Results and Discussion, oxidation of the nanoparticles leads to a solid-state conversion of Cu_2Se to the superionic conductor $Cu_{1.8}Se$ with a conductive coating. This, coupled with the variability in crystal structure and stoichiometry, makes Cu_2Se nanoparticles an interesting model system to investigate a mixed semiconducting and conducting nanocrystal film initially composed of the same compound.

Because of the flexibility present in the Cu_2Se family of compounds, both the structure and composition of the desired product must be controlled to tune the electronic and optical properties.[47] This control is exerted by carefully choosing the material synthesis procedure while simultaneously recognizing that the structure and stoichiometry are sensitive to the oxidation state of Cu as well as the high vapor pressure of Se.[48] We chose to pursue a one-pot solution-phase synthesis that provides control over the oxidation state of the constituent elements[49] as well as the size and morphology of the resulting nanoparticles.[29,50] It also offers a scalable, cost-effective route allowing for flexible processing aimed at device fabrication. Recently, nonstoichiometric $Cu_{2-x}Se$ nanocrystals via a one-pot synthesis have been reported and result in beautiful morphologies and narrow size distributions.[51,52] To our knowledge, this is the first reported one-pot solution-phase synthesis of stoichiometric Cu_2Se nanoparticles without the initial presence of the substoichiometric phase. Through drop-casting thin films of stoichiometric Cu_2Se nanoparticles, we developed the steps which allow the assembly of functional energy-related devices from a single material by controlling the surface oxidation and resulting solid-state conversion to $Cu_{1.8}Se$.

EXPERIMENTAL SECTION

Chemicals. Selenium powder (99.99%), copper acetate hydrate (98%), technical grade trioctylphosphine (TOP; 90%), trioctylphosphine oxide (TOPO; 99.9%), methyl isobutyl ketone (MIBK; 99+%), and ACS grade isopropyl alcohol (IPA; >99.5%) were purchased from Sigma-Aldrich. Octylphosphonic acid (OPA) was purchased from PCI Synthesis. Poly(methyl methacrylate) (PMMA) solutions, both 495K MW and 950K MW, were purchased from MicroChem. The chemicals were used as received without further purification. All anhydrous solvents were freeze−pumped−thawed to remove any dissolved oxygen prior to use.

Methods. Nanoparticles of Cu_2Se were prepared under inert conditions using standard Schlenk line and glovebox techniques.[50,53−57] In a typical synthesis, a mixture of 4.6 mmol of TOPO and 2 mmol of OPA in a 50 mL three-neck round-bottom flask was prepared in a nitrogen glovebox. Equipped with a stir bar, thermocouple, and reflux condenser, the reaction flask was sealed with rubber septa, and transferred to an Ar Schlenk line, where it was degassed at 70 °C and subsequently heated to 300 °C at a rate of 500 °C/h. In two separate vials, precursor solutions of copper (TOPCu) and selenium (TOPSe) were prepared in the glovebox by combining 1 mmol of copper acetate hydrate in 2.5 mmol of TOP and 1 mmol of selenium powder in 1.5 mmol of TOP. Both vials were sealed with rubber septa, and the as-prepared solutions were then taken out of the glovebox and sonicated until the selenium powder completely dissolved and the TOPCu became a light aqua green. After sonication, the TOPCu and TOPSe solutions were loaded into separate 2.5 mL gastight Luer Lock syringes and rapidly injected into the reaction flask containing the TOPO/OPA solution simultaneously. After injection, the growth temperature was lowered to 285 °C and the reaction was allowed to proceed for 13 min. The reaction was then quenched by injecting the product into degassed toluene.

Purification of the Cu_2Se nanoparticles was performed in the glovebox using degassed solvents to avoid surface oxidation. The resulting product solution was centrifuged in excess toluene for 20 min to remove any residual bulk product. The supernatant was decanted and transferred to another centrifuge tube, where 2.5 mL of acetonitrile was added, and the resulting murky-brown solution was centrifuged for another 20 min. The supernatant was again decanted and transferred to a fresh centrifuge tube. Methanol was then used to precipitate the remaining nanoparticles from the supernatant, which were subsequently redispersed in toluene. Methanol was added a second time to remove any excess surfactant, and the resulting Cu_2Se nanoparticles were stored in toluene for future characterization.

Transmission Electron Microscopy. Transmission electron microscopy (TEM) images and selected area electron diffraction (SAED) patterns were collected using a JEOL JEM-2000 transmission electron microscope under a working voltage of 160 kV. High-resolution TEM (HR-TEM) images were obtained with a Philips CM200 STEM instrument using a working voltage of 200 kV. The TEM samples were created by dipping a carbon-coated copper grid in a toluene solution containing the nanoparticles three times.

UV−vis. UV−vis spectra were collected for Cu_2Se thin films using an Agilent 8453 UV−vis ChemStation spectrophotometer. The thin films were prepared by drop-casting nanoparticles on quartz microscope slides inside a nitrogen glovebox, and the UV−vis spectrum was taken immediately after removal from the glovebox, and at 24 h, 48 h, 1 week, and 2 weeks of air exposure.

X-ray Diffraction. Powder X-ray diffraction (XRD) was performed on a Scintag X-2 advanced diffraction system equipped with Cu Kα radiation with a wavelength of 1.54 nm. Samples were prepared in the glovebox from a slurry of Cu_2Se nanoparticles in toluene. The samples were subsequently dried under inert conditions, and XRD patterns were taken immediately after removal from the glovebox as well as after 24 h, 48 h, 1 week, and 2 weeks of oxygen exposure.

X-ray Photoelectron Spectroscopy. X-ray photoelectron spectroscopy (XPS) spectra were obtained using a Physical Electronics ESCA 5800 system employing monochromatic Al Kα (E = 1486.6 eV) as the X-ray source. High-resolution scans were utilized to confirm the presence and provide information regarding the bonding environment and oxidation state of Cu and Se. These scans were performed with a pass energy of 23.5 eV and a step size of 0.10 eV/step. All spectra were shifted to account for sample charging using inorganic carbon as a reference to 284.80 eV.

Conductivity Measurements. Current−voltage ($I-V$) measurements were taken employing a two-probe method using a Compactstat electrochemical interface potentiostat with a step size of 2 mV and a scan rate of 2.5 mV/s. Devices were fabricated by spin-coating a layer of 495K MW PMMA, followed by a second layer of 950K MW PMMA, onto a silicon chip with a 100 nm thermal oxide layer. Electron beam lithography (EBL) was employed to draw electrodes spaced 500−600 nm apart. A developing solution of methyl isobutyl ketone and isopropyl alcohol in a 1:2 (v/v) ratio was subsequently used to develop the features. Approximately 20 nm of chromium and 80 nm of gold were evaporated onto the substrates. The chips were then submersed in acetone to remove the remaining PMMA. To avoid oxygen contamination, a suspension of Cu_2Se nanoparticles was drop-cast onto the chip in the glovebox following a procedure previously reported in the literature.[58] Briefly, a metal stub was placed in the center of a recrystallization dish, and 2 mL of degassed toluene was added. The substrate with the evaporated metal contacts was positioned on top of the stub, and 10 drops of the Cu_2Se nanoparticle solution was placed on the substrate. A watch glass covered the recrystallization dish to slow the evaporation rate. This process was repeated three times to ensure a uniform film of nanoparticles between the metal contacts. Current−voltage measurements of the nanocrystalline film were collected both in the glovebox and after the film was exposed to air.

RESULTS AND DISCUSSION

Parts a and b of Figure 1 contain representative TEM and HR-TEM images of Cu_2Se synthesized by simultaneously injecting TOPSe and TOPCu from separate syringes into the reaction flask at the same rate. This procedure produced monodispersed nanocrystals with a hexagonal morphology that arranged in a close-packed configuration. A characteristic SAED pattern of the nanoparticles (Figure 1a inset) is indexed to the (030), (060), (090), (012), and (402) reflections of monoclinic Cu_2Se. In addition, multiple lattice fringes were observed in the HR-TEM image contained in Figure 1b (inset). The measured spacings of 3.4, 2.3, and 2.1 Å correspond to the (060), (090), and (012) planes of monoclinic Cu_2Se, respectively, thereby corroborating the indexed SAED pattern. Particle size analysis performed on the sample yielded an average size of 10.1 ± 0.8 nm, corresponding to a monodispersity of 8.1% (Figure S1a, Supporting Information). However, as illustrated in Figure S1b, when the injection rate, sonication time, and injection and growth temperature were altered, monodispersed nanoparticles could not be synthesized. This result demonstrates that the above-mentioned synthesis conditions were the three key parameters that control the Cu_2Se nanoparticle nucleation and growth. Of the three, the most important aspect was temperature, as variation of both the injection and growth temperatures led to inconsistent results. This is because the injection temperature controls the particle nucleation kinetics.[59] In this case, the injection temperature must be high enough to immediately decompose the Cu and Se precursors, thereby promoting instantaneous nucleation of the desired nanoparticles. Nucleation was then followed by nanocrystal growth, which was also temperature dependent. This is due to the fact that the growth temperature controls the stability, diffusion rate, and binding strength of the surfactant to the growing nanocrystal surface, ultimately affecting the growth rate.[59] When the growth temperature was above 290 °C, uncontrolled growth occurred, leading to a bimodal size distribution. At temperatures below 275 °C, the growth rate was too slow, which also resulted in a broad size distribution. On the basis of these results, it was determined that an injection temperature

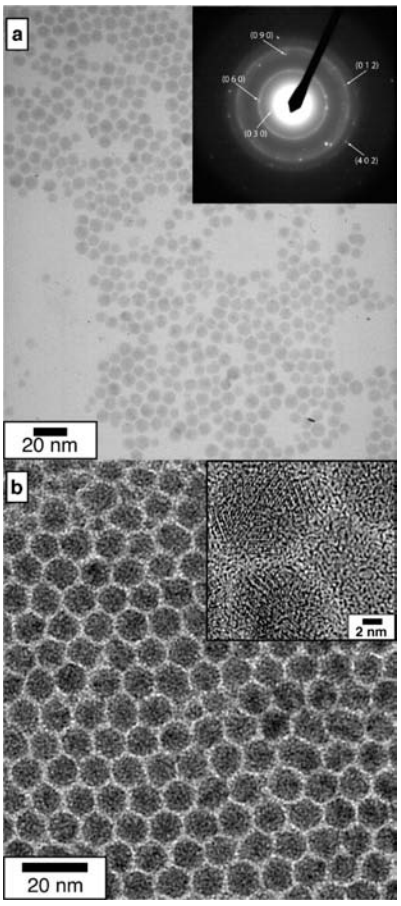

Figure 1. (a) TEM and (b) HR-TEM images of Cu_2Se nanoparticles synthesized via simultaneous injection of TOPSe and TOPCu. Inset a: SAED pattern of the nanoparticles indexed to stoichiometric monoclinic Cu_2Se. Inset b: HR-TEM image showing the crystallinity of the nanoparticles.

of 300 °C and a growth temperature of 285 °C were optimal for the synthesis of monodisperse Cu_2Se nanoparticles.

As observed with temperature, the nanoparticle size and size distribution were also functions of the precursor injection rate. When the injection rate was different for each precursor, a bimodal size distribution was observed. This is not surprising as different precursor injection rates would lead to a variation in the relative ratios of the Cu and Se precursors, ultimately inducing multiple nucleation events. Similar results were obtained when the TOPSe and TOPCu were combined into one syringe prior to injection. This could be attributed to heterogeneity of the combined precursor solution and/or a reaction occurring between the Cu and Se precursors before injection. The best results were obtained when TOPSe and TOPCu were in separate syringes but injected at the same time and rate. Because Cu_2Se is a promising candidate for photovoltaic applications, the transport properties of thin films fabricated by drop-casting solutions of Cu_2Se nanoparticles were measured.

Devices consisting of the Cu_2Se nanoparticles were assembled using EBL with a design similar to that employed by Bawendi and co-workers (Figure 2a).[60,61] Figure 2b contains a scanning electron micrograph of a chip showing three characteristic devices used for testing. The inset clearly shows a continuous Cu_2Se film of nanoparticles (darker gray middle region) bridging two Au electrodes (light gray outer regions). To ensure that the

dx.doi.org/10.1021/ja106254h |J. Am. Chem. Soc. 2011, 133, 1383–1390

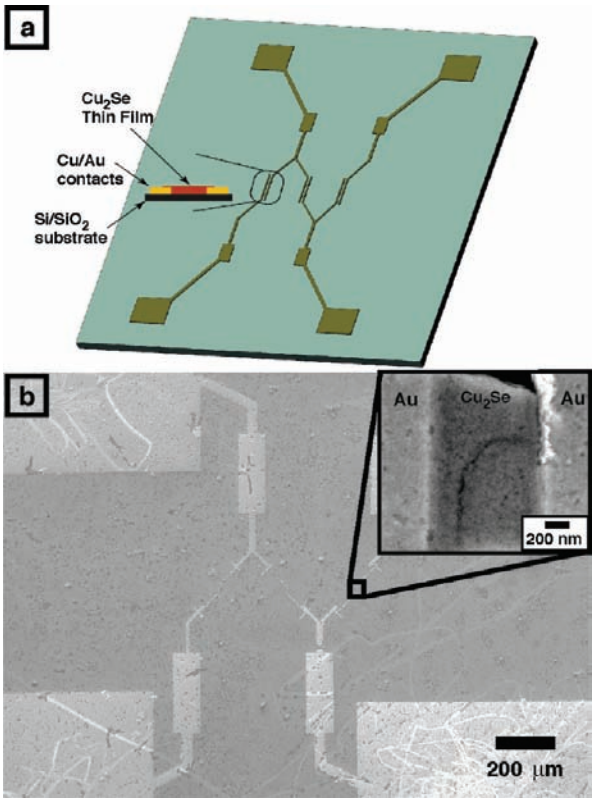

Figure 2. (a) Schematic representation of a Cu_2Se nanocrystal thin film device. (b) SEM micrograph of a device. The inset is a high-resolution image of the thin film overlying the two electrodes.

observed current came from the nanocrystalline film, current measurements as a function of voltage were collected from the SiO_2 substrate and the Au electrodes, resulting in open circuit and metallic behavior, respectively. To determine whether the electronic properties of a device containing Cu_2Se nanoparticles can be regulated through a time-controlled oxidation of the film, $I-V$ measurements were collected before and after exposure to the atmosphere.

The inset in Figure 3 contains plots of the current as a function of voltage collected from devices illustrated in Figure 2 that were protected in a nitrogen atmosphere prior to oxygen exposure. The symmetric S-shaped curve measured from the film is indicative of a semiconductor with a maximum current of ± 4 nA at ± 1 V. When kept in an inert environment, the current response remained unchanged over 48 h. The stability of the Cu_2Se nanoparticle thin film was then evaluated in air by measuring the $I-V$ response immediately after removal of the device from the nitrogen glovebox. The current response was subsequently evaluated hourly for 6 h. The data curves for the first seven measurements are plotted in Figure 3. The initial scan conducted outside the nitrogen glovebox exhibited semiconducting behavior with a slight increase in current to 5.4 nA, a difference of ca. 1.5 nA when compared to the 48 h measurement collected inside the box before the device was exposed to air. Similar results were obtained after 1 h of exposure to air with a doubling of the maximum current measured before air exposure. However, after 2 h of exposure, a substantial increase in current was observed and the $I-V$ curve transitioned to an almost linear response, indicating more ohmic than semiconducting behavior. As illustrated in Figures 3 and S2a (Supporting Information), this trend continued with an increase of almost 2 orders of magnitude in the current output after 6 h of air exposure. The ohmic response continued with a drastic rise in current to 5 μA after 24 h of air exposure and a slight increase to 6 μA after 48 h. The maximum current of 13.5 μA, a 3000-fold increase from the initial response, was observed after 1 week with a subsequent decrease to 6.5 μA after 2 weeks of exposure. The change in behavior from semiconducting to ohmic, as well as the increase in current response by over 3 orders of magnitude, demonstrated the potential to tune the electronic properties of Cu_2Se nanoparticles through controlled oxidation.

As mentioned above, it is well-known that Cu^+ in Cu_2Se can oxidize to Cu^{2+} when exposed to air, a process that is enhanced in nanoparticles due to a high density of surface sites. In addition to being highly reactive, nanoparticles allow one to monitor chemical and crystallographic changes that may not be observable in the bulk material. Using XRD and XPS techniques, the oxidatively induced changes in Cu_2Se as a function of exposure time to air were monitored to better understand the observed change in electronic properties. Beginning with a systematic XRD investigation, Cu_2Se samples were prepared in a nitrogen atmosphere to prevent oxidation. Once removed, an initial XRD pattern was immediately collected and the sample was then stored under ambient conditions between subsequent measurements for time intervals consistent with the electronic transport study (initial, 24 h, 48 h, 1 week, and 2 weeks). The XRD patterns are stacked in Figure 4 as a function of time to clearly show the transformation of the Cu_2Se nanoparticle crystal structure to $Cu_{1.8}Se$ when exposed to air.

The diffraction peaks in the initial pattern presented in Figure 4 have been indexed to monoclinic Cu_2Se (JCPDS 27-1131), thereby confirming the reflection assignments in the SAED pattern shown in Figure 1. All peaks could be assigned, suggesting that no crystalline impurities were present. There was a slight shift to higher 2θ for all peaks in the XRD pattern of the sample exposed to air for 24 h, indicating a decrease in the lattice parameters when compared to the initial sample. After 48 h, however, a shoulder was apparent at higher 2θ for the peak located at 44°, which became more pronounced as the exposure time increased. The shoulder eventually developed into a separate peak, while peaks corresponding to the copper-deficient $Cu_{1.8}Se$ began to emerge. After 2 weeks of exposure, all of the diffraction peaks were assigned to cubic $Cu_{1.8}Se$ (JCPDS 71-44), suggesting a complete solid-state conversion. This conversion is useful because $Cu_{1.8}Se$ is cubic, instead of monoclinic, and Cu deficient when compared to Cu_2Se. Because of these variations, the substoichiometric material also has different properties. The solid-state conversion to substoichiometric $Cu_{1.8}Se$ in conjunction with an approximate 3000-fold increase in conductivity clearly demonstrates that initially fabricating a functional device with stoichiometric Cu_2Se and controllably oxidizing it can result in films with tunable electronic properties.

To further understand the mechanism behind the solid-state conversion demonstrated by the time-resolved XRD analysis, a systematic XPS study was performed to investigate the oxidation states of both the Cu and Se atoms as a function time when exposed to air. The evolution of the Cu2p XPS spectra contained in Figure 5a as a function of exposure time shows a clear oxidation from Cu^+ to a mixture of Cu^+ and Cu^{2+}. As illustrated in Figure 5b, the initial $Cu2p_{3/2}$ and $Cu2p_{1/2}$ peaks were symmetric, narrow, and devoid of satellite peaks. This spectrum is indicative of monovalent copper. When the Cu_2Se sample was

dx.doi.org/10.1021/ja106254h |J. Am. Chem. Soc. 2011, 133, 1383–1390

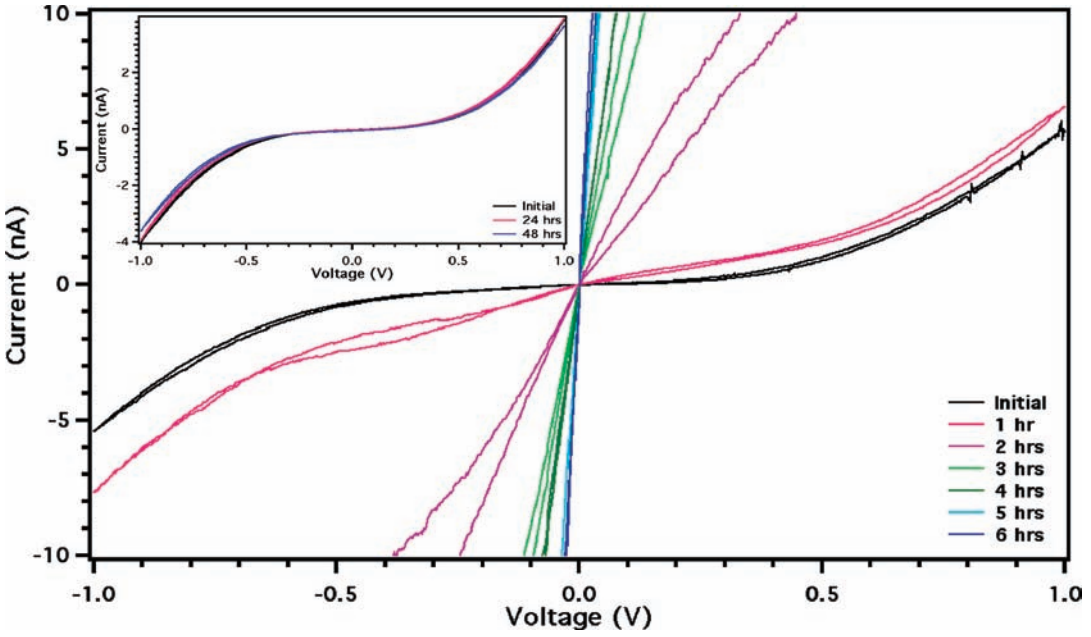

Figure 3. Current−voltage measurements of a Cu_2Se nanoparticle thin film taken as a function of time exposed to air. Measurements are taken immediately following removal from the glovebox and then once an hour for the subsequent 6 h. The inset illustrates the semiconducting behavior of the film when kept in an inert environment for the initial and 24 and 48 h current−voltage measurements recorded inside the glovebox.

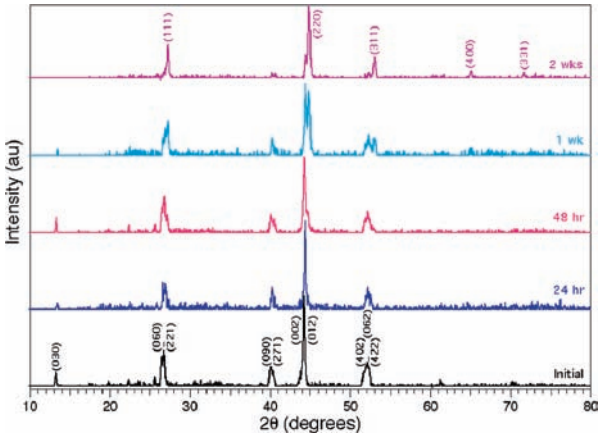

Figure 4. XRD patterns of Cu_2Se nanoparticles as a function of air exposure. The initial pattern was taken immediately after the sample was removed from the glovebox. That pattern is indexed to monoclinic Cu_2Se (JCPDS 27-1131). As the exposure time increases, the peaks shift to higher 2θ until the particles are converted to cubic $Cu_{1.8}Se$ (JCPDS 71-0044).

exposed to oxygen for 2 weeks, however, the Cu2p peaks in the spectrum contained in Figure 5c broadened and underwent splitting while pronounced satellite peaks formed due to paramagnetic Cu^{2+}. Since XPS is primarily a surface characterization technique, this dramatic change in the spectra can be attributed to the oxidation of a significant portion of the surface Cu^{+}, resulting in the presence of mixed valent $Cu^{+,2+}$.

The Se atoms were also evaluated using XPS techniques and underwent a similar conversion when exposed to oxygen. Figure 6a contains Se3d spectra that clearly show a shift to higher binding energy with an increase in exposure time. The Cu_2Se spectrum plotted in Figure 6b for a sample not exposed to oxygen contains $Se3d_{5/2}$ and $Se3d_{3/2}$ peaks, which, in addition to appearing symmetric and narrow, demonstrate the characteristic shape of Se^{2-} in a consistent bonding environment. That is, the $Se3d_{3/2}$ peak is at a binding energy 0.86 eV higher than that of the $Se3d_{5/2}$ peak, and the spin−orbital splitting ratio is 2:3.[62] The observed binding energy of 53.9 eV for the Se3d peak is also in agreement with what has been previously reported in the literature for Cu_2Se,[63] further confirming the indexed XRD and SAED patterns. However, once the sample was exposed to air for 2 weeks, the Se spectrum contained in Figure 6c showed two very distinctive peaks around 54 and 58.5 eV. The fitting of these peaks was evidence of multiple oxidation states ranging from the selenide to the oxide species. The evolution of the Cu and Se spectra was analyzed in more detail to shed light on the changing crystal structure and chemical composition of the nanoparticles.

An evaluation of the initial $Cu2p_{3/2}$ and $Se3d_{5/2}$ peak areas yielded a Cu to Se atomic ratio of 2.0:1.0, demonstrating that the initial sample was Cu_2Se. As the solid-state conversion progressed, for which the XPS spectra of Cu and Se are presented in panels a−e of Figures S3 and S4 (Supporting Information), respectively, the atomic ratio increased from an initial value of 2.0:1.0 to 5.2:1.0. A bar graph illustrating the evolution of the atomic ratio as a function of exposure time is plotted in Figure S3f. These data, coupled with the XRD analysis that indicated a solid-state conversion from Cu_2Se to $Cu_{1.8}Se$, suggested that solid-state diffusion of cationic Cu from the particle core to the surface occurred. This is not surprising because Se atoms are not mobile in this particular crystal structure while the diffusion of cationic Cu has been shown to be facile.[35,64−66] Consequently, as illustrated in Figure S3f, the surface Cu^{+} oxidized to Cu^{2+} upon exposure to oxygen, thereby establishing a chemical potential gradient that resulted in the diffusion of Cu^{+} from the particle core to the surface. Equilibrium was achieved when the conversion to more air-stable $Cu_{1.8}Se$ was complete, at which time ca. 80% of the surface Cu existed as Cu^{2+} likely in the form of conductive copper oxide (CuO), copper hydroxide ($Cu(OH)_2$), copper selenite ($CuSeO_3$), or their combination.[67,68]

dx.doi.org/10.1021/ja106254h |*J. Am. Chem. Soc.* 2011, 133, 1383–1390

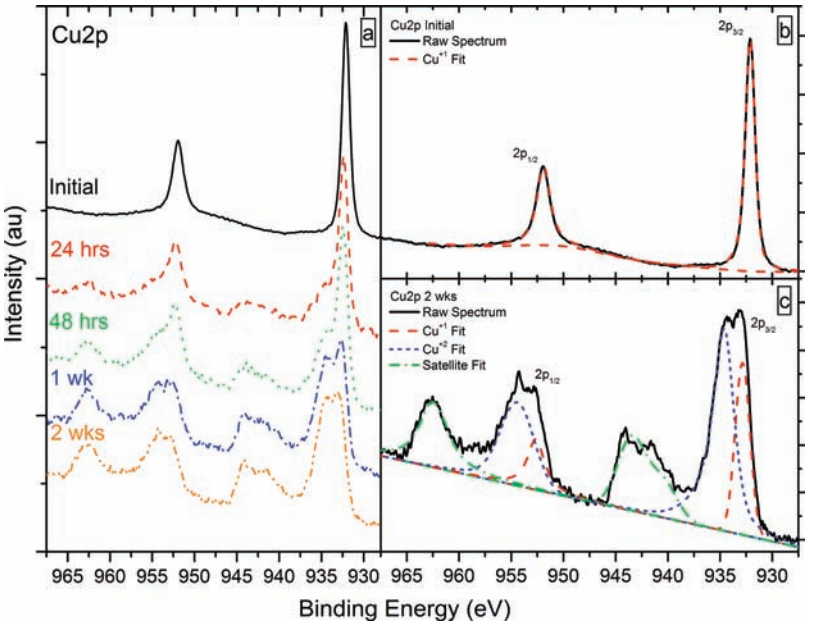

Figure 5. (a) Change in the Cu2p XPS spectra after exposure to oxygen. (b) Initial XPS spectrum of the Cu2p region as well as the $Cu2p_{3/2}$ and $Cu2p_{1/2}$ peak fits used to calculate atomic ratios. (c) XPS spectrum of the Cu2p region with peak fits for Cu^{+}, Cu^{2+}, and satellites due to the paramagnetic Cu^{2+} after the sample had been exposed to oxygen for 2 weeks.

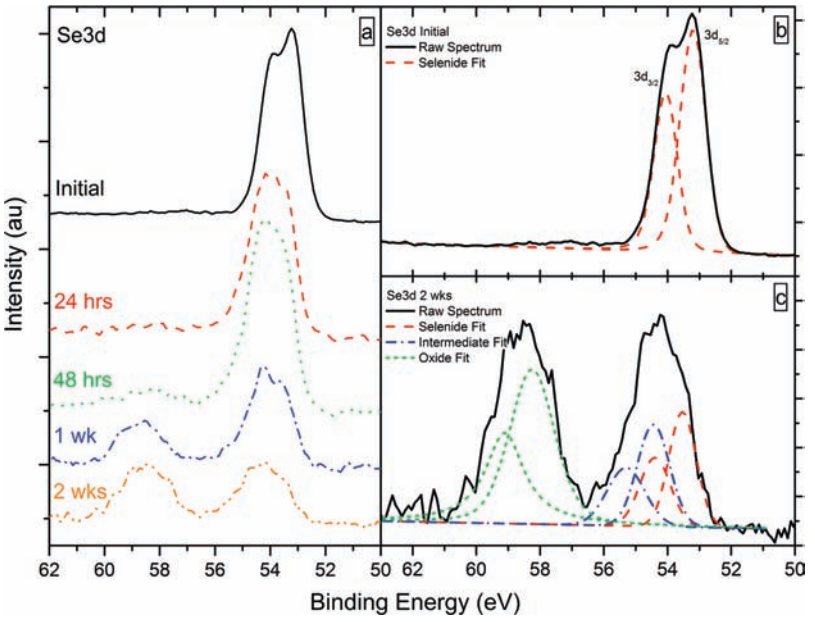

Figure 6. (a) Change in the Se3d XPS spectra after exposure to oxygen. (b) Initial XPS spectrum of the Se3d region as well as the $Se3d_{5/2}$ and $Se3d_{3/2}$ peak fits used to calculate atomic ratios. (c) Characteristic XPS spectrum of the Se3d region with Se^{2+} (due to the selenide), an intermediate oxidation state (roughly correlating to Se^{0}), and Se^{4+} (likely due to SeO_2) peak fits for the sample that had been exposed to oxygen for 2 weeks.

As with Cu, the Se atoms oxidized when exposed to oxygen. Initially, Se^{2-} was the only Se species present. In 24 h, however, ca. 45% of the selenide species was converted to an intermediate species with an oxidation state more positive than that of Se^{2-}, with a smaller percentage of ca. 5% being converted to Se^{4+}, tentatively identified as SeO_2. The intermediate Se species could be in the form of a polyselenide. With the formation of Cu−O adducts, a sufficient number of Cu−Se bonds have to be broken; the free Se atoms could then form short polyselenide (Se−Se−Se) chains on the surface, causing the shift in the XPS spectra to higher binding energy.[69] However, due to the complexity of the Se3d spectra for samples exposed to oxygen, relating the oxidation state of the intermediate species to an absolute binding energy was problematic as the binding energy shifts for different Se compounds are small.[62] Nonetheless, it was obvious when the spectra shown in Figure S4a−e (Supporting Information) were analyzed that, as the oxygen exposure time increased, Se was converted from the anion to the fully oxidized cation through an intermediate species. As illustrated in Figure S4f, a majority of the surface Se has been converted to the oxide

after 2 weeks of exposure while approximately equal amounts of the selenide and intermediate species were present. In bulk samples, the oxidation of both Cu and Se surface sites would have little effect on the physical and electronic properties of the material. However, when the size is reduced to the nanoscale, the effects of surface oxidation can alter both the physical and electronic properties. This was further elucidated in the optical properties of Cu_2Se, for which the UV−vis spectra are shown in Figure S5 (Supporting Information). Time-resolved UV−vis measurements show that after 24 h of air exposure the indirect band gap increases from 1.3 to 1.4 eV while the direct band gap increases from 2.2 to 2.4 eV. This change in band gap energy remains constant over 2 weeks and may explain the large variations in band gaps reported in the literature.[27,30−32] The dramatic changes observed in the time-resolved XRD and XPS data, coupled with the UV−vis data, are consistent with the changes observed in the electronic properties.

The XRD and XPS data contained in Figures 4−6 mimic the observed trends in the $I-V$ curves plotted in Figures 3 and S2 (Supporting Information). A Cu_2Se sample not exposed to oxygen is composed of Cu^+ and Se^{2-} with a Cu:Se ratio of 2.0:1.0 without a surface oxide layer. The semiconducting behavior is therefore dictated by the intrinsic properties of the Cu_2Se nanoparticles and the interparticle contact resistance. After 24 h of air exposure, however, the resistance dropped significantly, as indicated by a large increase in the maximum current. This behavior can be explained by the presence of conducting CuO and intermediate Se species on the surface of the nanoparticles as well as the solid-state conversion to the superionic conductor $Cu_{1.8}Se$. As the Cu was oxidized to Cu^{2+}, for which the surface Cu^+ decreased to ca. 50% of its original concentration in 24 h (Figure S2f), a chemical potential gradient was established within the particle. This resulted in the solid-state diffusion of cationic Cu from the particle core to the surface, making the particle core Cu deficient. As the Cu deficiency increased, more holes were generated, thereby increasing the majority charge carrier concentration.[68] As illustrated in Figure 4, equilibrium was reached when the particles were converted to the substoichiometric $Cu_{1.8}Se$. The drop in the maximum current from 1 to 2 weeks can be explained by the conversion of surface Se from an intermediate species to the oxide. As illustrated by Figure S4f (Supporting Information), the relative ratio of the fully oxidized species to the intermediate species became greater than 1 between 1 and 2 weeks. This is important because the binding energy of the Se intermediate is close to that exhibited by zerovalent Se, which provides more charge carriers at the expense of less energy than the oxide species. However, the formation of a significant Se surface oxide could increase the interparticle resistance and mitigate the increase in charge carriers generated within and on the surface of the particles due to the solid-state conversion and CuO formation, respectively.

CONCLUSIONS

A methodology has been created to implement the same material in energy-related devices as both the semiconducting and conductive domain by controllably tuning the electronic properties of Cu_2Se nanocrystals through time-resolved oxidation. To accomplish this, a synthesis procedure for monodispersed Cu_2Se nanoparticles without the presence of substoichiometric $Cu_{1.8}Se$ was developed for which three key variables for controlling size and size distribution were identified. Upon optimization of these parameters—injection temperature, growth temperature, and injection rate—reproducible, monodisperse Cu_2Se nanoparticles with a diameter of 10.1 ± 0.8 nm were synthesized. Thin film devices of these nanoparticles were subsequently prepared by drop-casting onto EBL-fabricated Au contacts. These devices initially demonstrated semiconducting behavior; however, after 1 week of exposure to oxygen, a 3000-fold increase in conductivity and a change to ohmic behavior was observed. XRD and XPS studies suggest the change in conductivity is due to Cu_2Se nanoparticles readily reacting with oxygen, ultimately leading to a solid-state conversion to $Cu_{1.8}Se$.

ASSOCIATED CONTENT

Supporting Information. Additional TEM images and size distribution plots, quantitative XPS analysis, extended current−voltage measurements, and UV−vis data. This material is available free of charge via the Internet at http://pubs.acs.org.

AUTHOR INFORMATION

Corresponding Author
Amy.Prieto@colostate.edu

ACKNOWLEDGMENT

This work was supported by start-up funds from Colorado State University. We thank Dr. Sandeep Kohli (XRD), Dr. Pat McCurdy (XPS), and Drs. Gary Zito and John Chandler at the Colorado School of Mines (TEM) as well as Mr. Vern Robertson from JEOL for technical assistance. TEM imaging was supported in part by the Microscope Imaging Network core infrastructure grant from Colorado State University.

REFERENCES

(1) Talapin, D. V.; Lee, J.-S.; Kovalenko, M. V.; Shevchenko, E. V. *Chem. Rev.* **2010**, *110*, 389–458.
(2) Kamat, P. V. *J. Phys. Chem. C* **2008**, *112*, 18737–18753.
(3) Hillhouse, H. W.; Beard, M. C. *Curr. Opin. Colloid Interface Sci.* **2009**, *14*, 245–259.
(4) Kamat, P. V. *J. Phys. Chem. C* **2007**, *111*, 2834–2860.
(5) Law, M.; Luther, J. M.; Song, Q.; Hughes, B. K.; Perkins, C. L.; Nozik, A. J. *J. Am. Chem. Soc.* 2008, *130*, 5974–5985.
(6) Luther, J. M.; Law, M.; Beard, M. C.; Song, Q.; Reese, M. O.; Ellingson, R. J.; Nozik, A. J. *Nano Lett.* **2008**, *8*, 3488–3492.
(7) Luther, J. M.; Law, M.; Song, Q.; Perkins, C. L.; Beard, M. C.; Nozik, A. J. *ACS Nano* **2008**, *2*, 271–280.
(8) Sykora, M.; Koposov, A. Y.; McGuire, J. A.; Schulze, R. K.; Tretiak, O.; Pietryga, J. M.; Klimov, V. I. *ACS Nano* **2010**, *4*, 2021–2034.
(9) Wu, Y.; Wadia, C.; Ma, W. L.; Sadtler, B.; Alivisatos, A. P. *Nano Lett.* **2008**, *8*, 2551–2555.
(10) Koo, B.; Patel, R. N.; Korgel, B. A. *Chem. Mater.* **2009**, *21*, 1962–1966.
(11) Zhong, H. Z.; Zhou, Y.; Ye, M. F.; He, Y. J.; Ye, J. P.; He, C.; Yang, C. H.; Li, Y. F. *Chem. Mater.* **2008**, *20*, 6434–6443.
(12) Basol, B. M.; Kapur, V. K.; Norsworthy, G.; Halani, A.; Leidholm, C. R.; Roe, R. *Electrochem. Solid-State Lett.* **1998**, *1*, 252–254.
(13) Koo, B.; Patel, R. N.; Korgel, B. A. *J. Am. Chem. Soc.* **2009**, *131*, 3134–3135.
(14) Panthani, M. G.; Akhavan, V.; Goodfellow, B.; Schmidtke, J. P.; Dunn, L.; Dodabalapur, A.; Barbara, P. F.; Korgel, B. A. *J. Am. Chem. Soc.* **2008**, *130*, 16770–16777.
(15) Tang, J.; Hinds, S.; Kelley, S. O.; Sargent, E. H. *Chem. Mater.* **2008**, *20*, 6906–6910.

(16) Guo, Q.; Hillhouse, H. W.; Agrawal, R. *J. Am. Chem. Soc.* **2009**, *131*, 11672–11673.
(17) Riha, S. C.; Parkinson, B. A.; Prieto, A. L. *J. Am. Chem. Soc.* **2009**, *131*, 12054–12055.
(18) Steinhagen, C.; Panthani, M. G.; Akhavan, V.; Goodfellow, B.; Koo, B.; Korgel, B. A. *J. Am. Chem. Soc.* **2009**, *131*, 12554–12555.
(19) Kameyama, T.; Osaki, T.; Okazaki, K.-i.; Shibayama, T.; Kudo, A.; Kuwabata, S.; Torimoto, T. *J. Mater. Chem.* **2010**, *20*, 5319–5324.
(20) Shavel, A.; Arbiol, J.; Cabot, A. *J. Am. Chem. Soc.* **2010**, *132*, 4514–4515.
(21) Katari, J. E. B.; Colvin, V. L.; Alivisatos, A. P. *J. Phys. Chem.* **1994**, *98*, 4109–4117.
(22) Tricoli, A.; Pratsinis, S. E. *Nat. Nanotechnol.* **2010**, *5*, 54–60.
(23) Haram, S. K.; Santhanam, K. S. V. *Thin Solid Films* **1994**, *238*, 21–26.
(24) Haram, S. K.; Santhanam, K. S. V.; Neumannspallart, M.; Levyclement, C. *Mater. Res. Bull.* **1992**, *27*, 1185–1191.
(25) Gurin, V. S.; Prokopenko, V. B.; Alexeenko, A. A.; Wang, S.; Prokoshin, P. V. *Mater. Sci. Eng., C* **2001**, *15*, 93–95.
(26) Machado, K. D.; de Lima, J. C.; Grandi, T. A.; Campos, C. E. M.; Maurmann, C. E.; Gasperini, A. A. M.; Souza, S. M.; Pimenta, A. F. *Acta Crystallogr., Sect. B* **2004**, *60*, 282–286.
(27) Al-Mamun; Islam, A.; Bhuiyan, A. H. *J. Mater. Sci.: Mater. Electron.* **2005**, *16*, 263–268.
(28) Jagminas, A.; Juskenas, R.; Gailiute, I.; Statkute, G.; Tomasiunas, R. *J. Cryst. Growth* **2006**, *294*, 343–348.
(29) Seoudi, R.; Shabaka, A. A.; Elokr, M. M.; Sobhi, A. *Mater. Lett.* **2007**, *61*, 3451–3455.
(30) Chen, W. S.; Stewart, J. M.; Mickelsen, R. A. *Appl. Phys. Lett.* **1985**, *46*, 1095–1097.
(31) Hermann, A. M.; Fabick, L. *J. Cryst. Growth* **1983**, *61*, 658–664.
(32) Okimura, H.; Matsumae, T.; Makabe, R. *Thin Solid Films* **1980**, *71*, 53–59.
(33) Abdullaev, G. B.; Aliyarova, Z. A.; Asadov, G. A. *Phys. Status Solidi* **1967**, *21*, 461–464.
(34) Ambade, S. B.; Mane, R. S.; Kale, S. S.; Sonawane, S. H.; Shaikh, A. V.; Han, S. H. *Appl. Surf. Sci.* **2006**, *253*, 2123–2126.
(35) Balapanov, M. K.; Zinnurov, I. B.; Mukhamed'yanov, U. K. *Russ. J. Electrochem.* **2007**, *43*, 585–589.
(36) Dhanam, M.; Manoj, P. K.; Prabhu, R. R. *J. Cryst. Growth* **2005**, *280*, 425–435.
(37) El Akkad, F.; Mansour, B.; Hendeya, T. *Mater. Res. Bull.* **1981**, *16*, 535–539.
(38) Hu, Y. X.; Afzaal, M.; Malik, M. A.; O'Brien, P. *J. Cryst. Growth* **2006**, *297*, 61–65.
(39) Itoh, K.; Usuki, T.; Tamaki, S. *J. Phys. Soc. Jpn.* **1998**, *67*, 3512–3516.
(40) Kashida, S.; Shimosaka, W.; Mori, M.; Yoshimura, D. *J. Phys. Chem. Solids* **2003**, *64*, 2357–2363.
(41) Ohtani, T.; Motoki, M.; Koh, K.; Ohshima, K. *Mater. Res. Bull.* **1995**, *30*, 1495–1504.
(42) Pai, R. R.; John, T. T.; Lakshmi, M.; Vijayakumar, K. P.; Kartha, C. S. *Thin Solid Films* **2005**, *473*, 208–212.
(43) Pathan, H. M.; Lokhande, C. D.; Amalnerkar, D. P.; Seth, T. *Appl. Surf. Sci.* **2003**, *211*, 48–56.
(44) Sklyarchuk, V. M.; Plevachuk, Y. O. *Semiconductors* **2002**, *36*, 1123–1127.
(45) Statkute, G.; Tomasiunas, R. *J. Appl. Phys.* **2007**, *101*, 113715−1–9.
(46) Gosavi, S. R.; Deshpande, N. G.; Gudage, Y. G.; Sharma, R. *J. Alloys Compd.* **2008**, *448*, 344–348.
(47) Schafer, A.; Kollwitz, M.; Ahlrichs, R. *J. Chem. Phys.* **1996**, *104*, 7113–7121.
(48) Wang, W. Z.; Yan, P.; Liu, F. Y.; Xie, Y.; Geng, Y.; Qian, Y. T. *J. Mater. Chem.* **1998**, *8*, 2321–2322.
(49) Puntes, V. F.; Krishnan, K. M.; Alivisatos, A. P. *Science* **2001**, *291*, 2115–2117.
(50) Peng, X.; Manna, L.; Yang, W.; Wickham, J.; Scher, E.; Kadavanich, A.; Alivisatos, A. P. *Nature* **2000**, *404*, 59–61.
(51) Choi, J.; Kang, N.; Yang, H. Y.; Kim, H. J.; Son, S. U. *Chem. Mater.* **2010**, *22*, 3586–3588.
(52) Deka, S.; Genovese, A.; Zhang, Y.; Miszta, K.; Bertoni, G.; Krahne, R.; Giannini, C.; Manna, L. *J. Am. Chem. Soc.* **2010**, *132*, 8912–8914.
(53) Manna, L.; Scher, E. C.; Alivisatos, A. P. *J. Am. Chem. Soc.* **2000**, *122*, 12700–12706.
(54) Millron, D. J.; Hughes, S. M.; Cui, Y.; Manna, L.; Li, J.; Wang, L.; Alivisatos, A. P. *Nature* **2004**, *430*, 190–195.
(55) Murray, C. B.; Norris, D. J.; Bawendi, M. G. *J. Am. Chem. Soc.* **1993**, *115*, 8706–8715.
(56) Peng, X.; Wickham, J.; Alivisatos, A. P. *J. Am. Chem. Soc.* **1998**, *120*, 5343–5344.
(57) Qu, L.; Peng, Z. A.; Peng, X. *Nano Lett.* **2001**, *1*, 333–337.
(58) Park, J.; Lee, S.; Lee, H. H. *Org. Electron.* **2006**, *7*, 256–260.
(59) Yin, Y.; Alivisatos, A. P. *Nature* **2005**, *437*, 664–670.
(60) Morgan, N. Y.; Leatherdale, C. A.; Drndic, M.; Jarosz, M. V.; Kastner, M. A.; Bawendi, M. *Phys. Rev. B* **2002**, *66*, No. 075339−075348.
(61) Porter, V. J.; Mentzel, T.; Charpentier, S.; Kastner, M. A.; Bawendi, M. G. *Phys. Rev. B* **2006**, *73*, 155303–155312.
(62) Moulder, J. F.; Stickle, W. F.; Sobol, P. E.; Bomben, K. D. *Handbook of X-ray Photoelectron Spectroscopy: A Reference Book of Standard Spectra for Identification and Interpretation of XPS Data*; Physical Electronics, Inc.: Chanhassen, MN, 1995.
(63) Cahen, D.; Ireland, P. J.; Kazmerski, L. L.; Thiel, F. A. *J. Appl. Phys.* **1985**, *57*, 4761–4771.
(64) Balapanov, M. K.; Yakshibaev, R. A.; Mukhamed'yanov, U. K. *Phys. Solid State* **2003**, *45*, 634–638.
(65) Bikkulova, N. N.; Stepanov, Y. M.; Mikolaichuk, A. N. *Russ. J. Electrochem.* **2007**, *43*, 595–597.
(66) Skomorokhov, A. N.; Trots, D. M.; Knapp, M.; Bickulova, N. N.; Fuess, H. *J. Alloys Compd.* **2006**, *421*, 64–71.
(67) Folmer, J. C. W.; Jellinek, F. *J. Less-Common Met.* **1980**, *76*, 153–162.
(68) Sykora, M.; Koposov, A. Y.; McGuire, J. A.; Schulze, R. K.; Tretiak, O.; Pietryga, J. M.; Klimov, V. I. *ACS Nano* **2010**, *4*, 2021–2034.
(69) Ogorelec, Z.; Celustka, B. *J. Phys. Chem. Solids* **1969**, *30*, 149–155.